Journal of Wind Engineering & Industrial Aerodynamics 279 (2026) 106615

Contents lists available at ScienceDirect

Journal of Wind Engineering & Industrial Aerodynamics

journal homepage: www.elsevier.com/locate/jweia

A post-disaster investigation of tornado impact on built-up area: A forensic engineering perspective

Yang Lei [a,b], Xiao Li [a,b,*], Guanzhong Wang [a,b], Bowen Yan [a,b], Xu Zhou [a,b], Qingshan Yang [a,b], Shenming Fu [c], Noram Irwan Ramli [d], Yingzhu Meng [a,b], Haile Li [a,b]

[a] School of Civil Engineering, Chongqing University, Chongqing, 400045, China
[b] State Key Laboratory of Safety and Resilience of Civil Engineering in Mountain Area, Chongqing, 400045, China
[c] State Key Laboratory of Earth System Numerical Modeling and Application, Institute of Atmospheric Physics, Chinese Academy of Sciences, Beijing, 100029, China
[d] Faculty of Civil Engineering Technology, University Malaysia Pahang Al-Sultan Abdullah, Pahang, 26300, Malaysia

ARTICLE INFO

Keywords:
Tornadoes
Field survey
Wind-induced disaster
Enhanced Fujita scale
Wind-borne debris

ABSTRACT

This paper presents a forensic investigation of the tornado that attacked Dongming, China, on July 5th 2024, based on an extensive post-disaster field survey. The tornado reached EF3 intensity according to the EF-scale and its adaptations, with a path 12 km in length and 690 m in maximum width. Analysis of substantial facade damage observed from a cluster of high-rise buildings revealed significant wind interference effects. Mechanisms behind the severe damage to brick-timber buildings, light steel structures, utility poles, a transmission tower, and trees were discussed in detail. Particular emphasis was placed on wind-borne debris, with lift-off speeds and trajectories analyzed based on field observations. The findings highlight the correlations of the tornado-induced damage with building cluster layout, structural resistance, debris motion, etc. This study aims to present valuable insights into the effects of intense tornadoes on built-up areas, providing strategies to enhance urban resilience against extreme wind events.

1. Introduction

Windstorm disasters inflict devastating socioeconomic impacts, ranking first in economic costs and second in global mortality among natural hazards. According to the World Meteorological Organization (WMO), extreme wind events account for 52% of direct economic losses (1.9 trillion U.S. Dollars, USD) and 39% of natural hazard-related fatalities (785,000 death cases) (Esri, 2023). Extreme wind events including tornadoes, downbursts, and tropical cyclones (as known as typhoons and hurricanes) are the primary sources of these high-intensity destruction (Li et al., 2021; Calotescu et al., 2024; Braik and Koliou, 2025). In particular, as revealed by the Emergency Events Database (EM-DAT) (EMDAT, 2023), tornadoes contributed to 5% of global natural disaster-induced economic losses between 2010 and 2022, with an estimated annual frequency toll of 2000 to 2500 and economic losses of approximately 3 to 4 billion USD. In the United States, where tornadoes are frequently reported, from 1994 to 2023, an average of 1200 events occurred each year (NOAA, 2023), with annual economic losses exceeding 2 billion USD (National Weather Service (NWS), 2023). In Europe, from 2005 to 2019, tornado occurrences averaged around 250 annually, with economic losses ranging from 2 to 3 billion Euros (approximately 2.3 to 3.5 billion USD) (Grieser and Haines, 2020). In China, from 2007 to 2017, tornado events occurred approximately 40 times annually, with economic losses exceeding 900 million Chinese Yuan (approximately 126 million USD) (Xu et al., 2024). Over the past decades, severe tornadoes have been observed across the world. The "Dixie Outbreak" in the southeastern United States, which occurred on April 27th 2011 and spawned 199 tornadoes across 16 states within 24 h, including 25 high-intensity tornadoes that caused 316 deaths (Doswell et al., 2012). On May 22nd 2011, the EF5 tornado attacked Joplin, Missouri, the United States, destroying over 5000 structures and caused 158 fatalities (Prevatt et al., 2012). On June 23rd 2016, an EF4 tornado in Yancheng, Jiangsu Province, China, caused damage to approximately 3000 buildings and 98 fatalities (Meng et al., 2018).

Compared to synoptic-scale weather systems like tropical cyclones, tornadoes, as micro-scale events, are characterized by their sudden

This article is part of a special issue entitled: INDAER_APCWE10 published in Journal of Wind Engineering & Industrial Aerodynamics.

* Corresponding author. School of Civil Engineering, Chongqing University, Chongqing, 400045, China.
E-mail address: lixiao_seanli@cqu.edu.cn (X. Li).

https://doi.org/10.1016/j.jweia.2026.106615
Received 26 March 2026; Received in revised form 5 July 2026; Accepted 17 August 2026
Available online 8 September 2026
0167-6105/© 2026 Elsevier Ltd. All rights are reserved, including those for text and data mining, AI training, and similar technologies.

occurrence, localized impact, and short lifespan. These factors make it difficult to predict their formation and movement, complicating real-time wind field observation and forecasting. As a result, opportunities to collect wind field data during the tornadoes are considerably rare in practice, and post-event disaster investigation through field surveys, also known as forensic engineering, usually serves as the sole means to investigate the near-ground wind field characteristics of tornadoes. These post-event investigations estimate the wind intensity based on the extent of wind-induced damage to objects such as structures (Yang et al., 2024) and vegetation (Meng et al., 2018). Prof. T.T. Fujita from the University of Chicago made an important attempt to qualitatively categorize the intensity of a tornado into different scales according to the damage it induces, and such method has been referred to as the Fujita Scale (F-scale) (Fujita, 1981). Following such approach, the Enhanced Fujita Scale (EF-Scale) was proposed by Texas Tech University in the 2006 (Texas Tech University Wind Science and Engineering Center, 2006), which is more systematic as it incorporates damage indicators (DI) and degrees of damage (DoD) for a more refined and precise wind intensity evaluation. As tornado characteristics have been further investigated, more countries and regions have developed their own adapted versions of EF-Scale, such as the Chinese EF-Scale (ChnEF) (Tornado intensity scale: GB/T 40243-2021, 2021; Technical specifications for tornado damage, 2017) and Japanese EF-Scale (JEF) (Japan Meteorological Agency, 2015), and Canadian EF-Scale (Sills et al., 2014).

It is worth noting that a few researchers have established empirical or semi-analytical methods for estimating threshold wind speeds by analyzing the mechanical mechanisms of specific DIs, such as vehicle overturning (Haan et al., 2017), roof uplift failure (Prevatt et al., 2012; Haan et al., 2010), road sign failure (Chmielewski et al., 2013), and collapse of utility poles (Braik et al., 2019) and transmission towers (Zhang et al., 2024). These methods often involve experimental tests and models to determine the critical wind speed, quantifying the near-ground wind field distribution. Post-disaster field surveys documenting the displacement of haybales, construction materials, vehicles, and large appliances are frequently used to reconstruct the horizontal trajectory distance and initial location of wind-borne debris, providing first-hand evidence for trajectory forecast and lift-off speed estimation. Based upon these observations, researchers such as Miller et al. (2024), Rotunno and Bluestein (2024) have integrated field evidence with tornado flow models to estimate plausible lift-off wind-speed ranges for different debris types.

Besides the damage collected from artificial objects such as civil structures and vehicles mentioned above, treefall damage observed through aerial and/or satellite imagery (Sills et al., 2020; Karstens et al., 2013) has also been utilized as a useful source to estimate the tornado intensity. Considering the uncertainties in treefall mechanisms, recent approaches emphasize the observation of overall treefall pattern utilizing the proportion of fallen trees to estimate the EF rating of the area, rather than relying on single tree-fall cases subjected to high randomness. Karstens et al. (2013) and Lombardo et al. (2015) conducted a digital analysis of aerial images from the Joplin tornado, identifying features of radial convergence zones and tangential rotation zones, thereby estimating the tornado path and wind field structure. Godfrey and Peterson (2017) also found that fallen trees within the tornado path formed converging and tangential patterns, consistent with the characteristic near-ground wind field structure of tornadoes. By adopting multiple samples of treefall cases to reveal the patterns of tree uprooting and fall directions in a specific region, such approach significantly reduces the randomness associated with individual treefall cases, serving as an important method for reconstructing near-surface wind speeds and wind field patterns.

It is important to note that the tornado damage is not solely attributed to extreme wind loads, but also to the significant impact forces exerted by wind-borne debris (WBD) driven by intense winds. The wind-borne debris is mobilized when near-surface winds exceed object-specific lift-off velocities, propelling objects into destructive aerodynamic trajectories. These projectiles may inflict devastating impacts on structures, vehicles, and human bodies during transit, triggering cascading damage chains that amplify socioeconomic losses. Wills et al. (2002) categorized debris into three types according to their geometric features, namely compact, plate-like, and rod-like, each presenting different aerodynamic behaviors. However, the WBD damage to objects (e.g., building cladding systems) has not been commonly considered as a DI for wind intensity estimation, despite there is clearly a physical linkage between the kinetic energy of WBD impact and the wind speed.

In recent years, the integration of post-disaster surveys, wind tunnel experiments, and numerical simulations has significantly advanced the study of WBD dynamics and impact damage, contributing significantly to the reconstruction of tornado wind fields and the vulnerability assessment of structures (Jain et al., 2020; Bourriez et al., 2020; Baker and Sterling, 2018). Models of WBD trajectories and lift-off probabilities, based on analytical tornado fields and Monte Carlo simulations (Moghim et al., 2015), are widely used to estimate wind speed and impact velocity distributions, aiding forensic wind speed reconstruction. Additionally, debris collision analysis coupling the computational fluid dynamics and the finite element method has enabled more accurate simulations of the impact process, providing insights into structural response and failure (Ai et al., 2023). Wind tunnel tests have also been conducted over the years, such as those by Texas Tech University and National Institute of Standards and Technology (Lin et al., 2007; Holmes et al., 2006; Simiu and Potra, 2011), to establish debris impact resistance standards for various materials and systems, highlighting the significant role of debris type and wind field characteristics in determining the extent of structural damage.

At approximately 14:30 Beijing Time (BJT, i.e., Coordinated Universal Time + 8 h) on July 5th 2024, an intense tornado attacked Dongming, China, resulting in 5 fatalities, 88 injuries, and 2820 damaged structures. Through conducting a post-disaster investigation of this tornado, this study analyzes the damage induced by both the extreme wind load and the WBD impacts. The paper is structured as follows: Section 2 presents the meteorological background and field survey setup; Section 3 reconstructs the tornado evolution, including the variations of its path and intensity, according to the observed wind-induced damage cases; Section 4 reveals the mechanisms behind the damage to different structures (i.e., high-rise buildings, brick-timber low-rise buildings, and light steel structures), power distribution infrastructures (i.e., utility poles and a transmission tower), and trees caused by the violent tornado winds; Section 5 investigates the motion of WBD, including their lift-off speeds and trajectories within the tornado wind field.

2. Meteorological background and survey setup

2.1. Meteorological background

Tornadoes emerge from severe convective weather systems with strong dynamic lifting, pronounced vertical wind shear, and abundant low-level moisture. Fig. 1 presents the sea level pressure over China at 14:00 BJT on July 5th, 2024. As showing that a surface low-pressure trough extended northeastward covered eastern China. As shown in the figure, the surface low-pressure trough stretching northeastward covered eastern China, providing favorable environment for the occurrence of extensive convective activity. Meanwhile, the northwestern periphery of the subtropical high transports warm and moist westerly airflow, while the cold high-pressure system adverts cold and dry leeward airflow southward. The prominent thermal and moisture contrast between warm and cold air masses forms an intense low-level convergence zone. The low-level jet further boosts the supply of moisture and energy in the troposphere, and Dongming was situated within this strong low-level convergence zone. Radar observations by local meteorological bureau revealed a clear tornado vortex signature at low

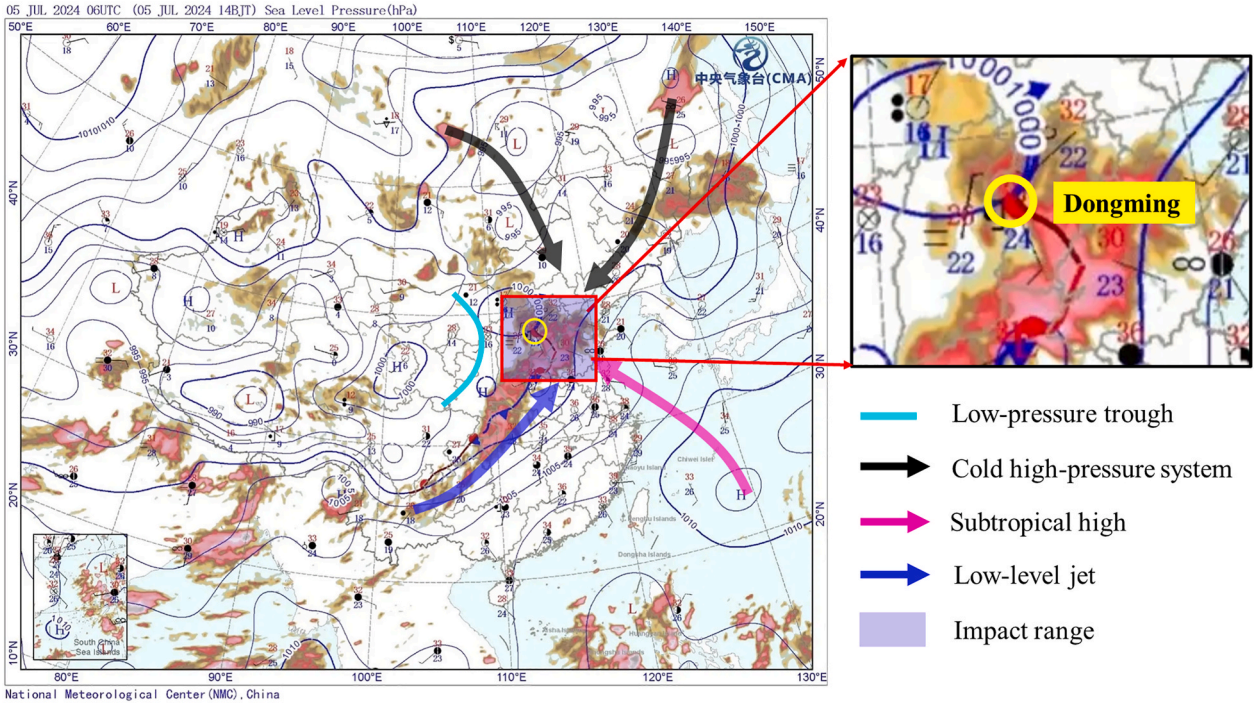

Fig. 1. Sea level pressure pattern shortly prior to tornado formation.

elevation angles, confirming the tornadic nature of the extreme wind event occurred in Dongming (Hou et al., 2025).

2.2. Field survey setup

Within 2 h after the tornado occurred in Dongming, the Wind-related Disaster Investigation (WDI) Group was alerted and immediately initiated its rapid response procedures. Operating under the Committee of Wind Disaster Mitigation and Energy Utilization Committee, China Association for Engineering Construction Standardization, the WDI Group comprises professionals specializing in wind damage analysis from both academic and industry fields. Preliminary information collected from

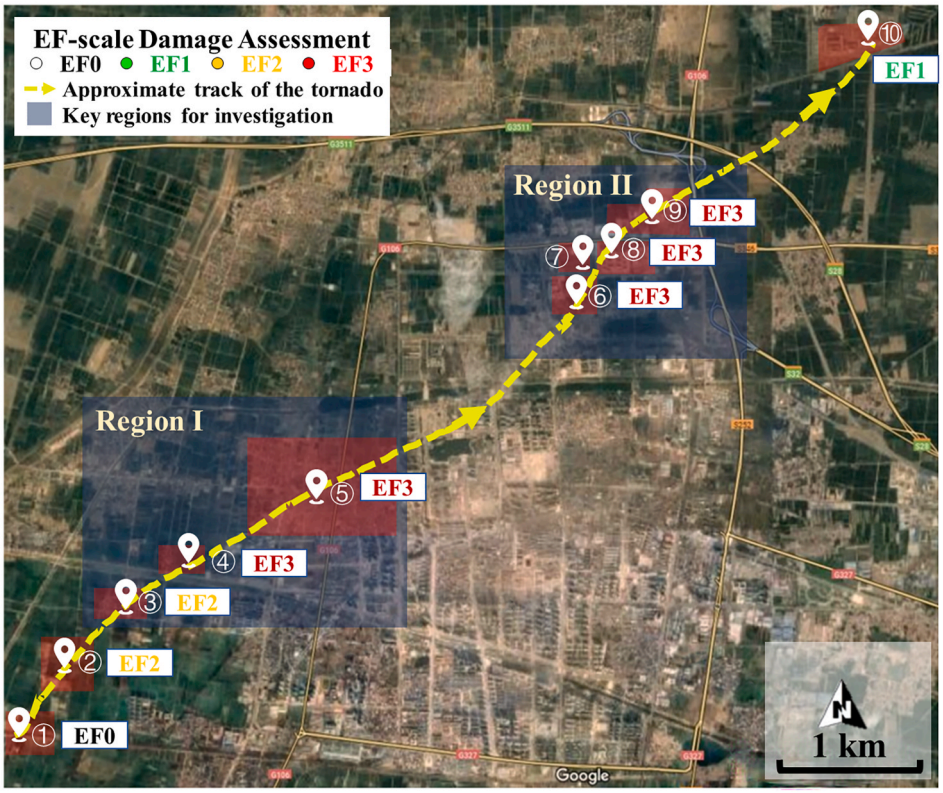

Fig. 2. Map of investigated areas and tornado path. (Imagery © 2025 Airbus, CNES/Airbus, Landsat/Copernicus, Maxar Technologies, Map data © 2025).

meteorological offices, local contacts, and public social media platforms indicated that the tornado was of considerable intensity, thereby meeting the criteria for launching a field damage survey.

In response to the call from the WDI Group, a survey team from Chongqing University was promptly dispatched and arrived in Dongming the following day. The team was equipped with a variety of survey tools, including a DJI Phantom 4 Pro V2.0 drone (i.e., unmanned aerial vehicle) instrumented with a 20-megapixel 4K CMOS image sensor. Reconnaissance across the city identified ten key areas affected by the tornado, labeled as Areas ① to ⑩ in Fig. 2, which were subsequently selected for detailed investigation. In these areas, over 400 damage cases of engineered structures were documented, including 15 high-rise buildings, approximately 350 low-rise (single- and two-story) brick-timber structures, over 10 light steel structures, 20 utility poles, a transmission tower, among others. Damage to other important objects, such as vegetation and vehicles, were also documented. In addition, over 20 witness interviews were conducted to gather observational information and visual records (e.g., video footage) of the tornado, providing supplementary evidence on the tornado evolution and the damage process.

3. Tornado evolution assessment

The evolution of the tornado, including variations in its intensity and path, was assessed primarily using the Enhanced Fujita Scale, EF-scale (Texas Tech University Wind Science and Engineering Center, 2006), its Chinese adaption, ChnEF-scale (Tornado intensity scale: GB/T 40243-2021, 2021; Technical specifications for tornado damage, 2017), as well as its Japanese adaption, JEF-scale (Japan Meteorological Agency, 2015). As introduced above, these scales evaluate tornado wind intensity according to the observations of damage indicators (DIs) and their associated degrees of damage (DoD). Table 1 presents ground-level and aerial photographs of representative DIs in the surveyed areas. Using the corresponding DoD of these DIs defined in the three scales, the maximum 3-s gust speed in these areas during the tornado's passage were estimated. Additionally, photographs and videos provided by witnesses and retrieved from public social media platforms were collected to provide direct visual evidence of the tornado evolution, confirming its counterclockwise rotation and its northeasterly track across Dongming. Based on the above findings, the tornado evolution is reconstructed as follows.

At around 14:20 on July 5th 2024 BJT, the tornado touched down in Area ① over an open field, where a few trees with a Diameter at Breast Height (DBH, i.e., 1.4 m above ground) less than 10 cm were found fallen, indicating an estimated intensity of EF0. The tornado intensified as it moved northeastward and reached Area ②, where progressive damage was observed. The roof of warehouses was destroyed at the edge of Area ② (EF1), and a truck weighing around 4.5 tons was overturned in the central part of Area ② (JEF2). Continuing to intensify along its northeasterly path, the tornado passed over a large farmland in Area ③, where the roof tiles of many single- and two-story brick-timber residential houses were found uplifted (EF2, ChnEF1, JEF2). In addition, a few trees with a DBH of around 20 cm were uprooted and suffered branch breakage. Subsequently, the tornado reached Area ④ and caused the collapse of a transmission tower approximately 20 m in height (EF3, ChnEF3). Observations in Area ⑤ revealed extensive structural failures among numerous low-rise residential houses, including uplifted roofs and collapsed exterior walls (EF3, ChnEF3, JEF3), as well as toppled 8-m-tall reinforced-concrete utility poles (EF3, ChnEF3, JEF2). Subsequently, the tornado caused collapse of 8 tower cranes and several manufactured double-wide houses in Area ⑥, subsequently the uplifted a large area of roof-mounted solar panels in Area ⑦, whilst the wind intensities were not estimated in these areas due to the absence of corresponding DIs in the current versions of EF-scale and ChnEF-scale, and JEF-scale. As the tornado arrived Area ⑧, a cluster of high-rise residential buildings sustained severe facade damage induced both by excessive wind loads and the impact of WBD (EF2, ChnEF3), and several trees with a DBH exceeding 15 cm were snapped (EF2, ChnEF2, JEF2). In Area ⑨, the sheet metal roofs of several industrial factory buildings were partially or entirely removed (EF3, ChnEF3, JEF3). Continuing northeastward, the tornado caused relatively moderate damage cases in Area ⑩, such as loss of the roofing materials failures, indicating a weakening in its intensity upon reach this area (EF1, ChnEF1, JEF2). No more damage cases were observed beyond Area ⑩, suggesting that the tornado rapidly dissipated after passing over this area. The total path length of the tornado was approximately 12 km, as plotted in Fig. 3.

Fig. 3 (a) and (b) illustrate the spatial distribution of damage cases in two regions, referred to as Region I (covering Areas ③ to ⑤) and Region II (⑥ to ⑨). In both figures, the location of each DI and its associated DoD are marked. Collapsed tower cranes, although not classified as DIs in the three scales, are also indicated in the figure because such damage is of significance. In addition, treefall orientations, that can be used for inferring wind directions (Sills et al., 2020; Karstens et al., 2013; Lombardo et al., 2015; Godfrey and Peterson, 2017) are recorded as well. Based on these damage cases, it is estimated that the maximum tornado path width reached approximately 500 m in Region I and 690 m in Region II.

4. Damage mechanisms

4.1. Damage to high-rise building cluster

As tornadoes mostly occur in rural and suburban areas, their damage to low-rise buildings, which is the dominant building type in these areas and typically single- or two-story residential buildings, has been well documented in existing damage surveys. However, records of tornado damage to high-rise buildings (say, over 25 m in height) are still lacking, so that the knowledge of tornado-resistant performance of these buildings remains very limited. In this study, the tornado traversed a cluster of high-rise buildings in Area ⑧, providing a unique opportunity to investigate its effects on these buildings.

Fig. 4 presents the layout of the high-rise building cluster and the inferred track of the tornado center. The cluster comprised 15 high-rise buildings, labeled as Buildings #1 to #15, with similar or identical exterior geometries, i.e., 28 m in height, 12 m in width, and lengths of either 40 m or 60 m. The tornado track near and within the cluster area was inferred from the damage cases observed at four locations, referred to as Locations A to D in the figure. The treefall in a converging pattern at Location A (Fig. 4(a)) and the wall collapsed in opposite directions at Location B (Fig. 4(b)) indicated that the tornado center passed directly over them, and such inference was confirmed by a video footage, available on open social media, capturing the entire tornado passage in the building cluster area. The footage also provides clear visual evidence that the tornado passed directly over Building #1 at Location C (Fig. 4 (c)), which is a rarely documented occurrence. As the tornado continued moving northeastward, it exited building cluster area at Location D, where signature convergence toward the tornado center due to radial winds and a radial treefall pattern caused by tangential winds were observed (Fig. 4(d)).

Although all 15 buildings remained structurally intact after the tornado strike, their facades experienced notable damage. Fig. 5(a) illustrates the damage on the south facade of Building #5, showing substantial failure of the cladding system, including glass windows and the thermal insulation layer (TIL) on the exterior walls. As presented in the figure, two distinct glass damage patterns were observed. The first pattern is the complete removal of the window, in which both the glass and the window frame were detached from the building after the frame reached its ultimate capacity under excessive wind loading. The second pattern involves partial fracture of the glass and is characteristic of WBD impact, i.e., debris perforated the glass without causing frame detachment. It is noteworthy that the first damage pattern does not preclude earlier debris impact, as debris-induced fracture on the glass may have

Table 1
Estimated wind intensity in key areas.

Area	①–②	②	③	④	⑤
Case	Warehouse 	High-sided truck 	Low-rise buildings 	Transmission tower 	Low-rise buildings 
Damage Indicator (DI)	EDI-23: Warehouse Building ChnDI: Metal-framed Agricultural Buildings	JDI-15: Large Vehicles	EDI-2: One-And Two-Family Residence ChnDI: Non-frame Residential Buildings JDI-1: Residential Housing	EDI-24: Electrical Transmission Line ChnDI: Transmission Tower	EDI-2: One-And Two-Family Residence ChnDI: Non-frame Residential Buildings JDI-1: Residential Housing
Degree of Damage (DoD)	EDI-23-DoD-4: Roof structure completely collapsed. ChnDoD: Complete building overturning	JDI-15-DoD-1: Overturning	EDI-2-DoD-4: Uplift of roof deck and loss of significant roof covering material (>20%) ChnDoD: Extensive damage to the roof JDI-1-DoD-7: Detachment of roof components	EDI-24-DD-6: Collapsed metal truss towers ChnDoD: Metal tower collapse	EDI-2-DoD-8: Most walls collapsed, except small interior rooms ChnDoD: Collapse of external walls JDI-1-DoD-8: Major Frame Structure Damage
3-s Gust Speed (m/s)	EF 39-54 ChnEF 37-53	JEF 45-65	EF 36-52 ChnEF 38-52 JEF 50-75	EF 52-74 ChnEF 52-74	EF 57-80 Chn EF 55-74 JEF 55-85
Estimated Intensity	EF1 ChnEF1	JEF2	EF2 ChnEF1 JEF2	EF3 ChnEF3	EF3 ChnEF3 JEF3
Area	⑤	⑧	⑧	⑨	⑩
Case	Utility poles 	High-rise concrete buildings 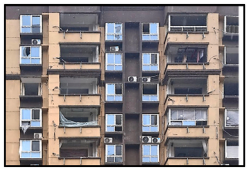	Trees 	Industrial factory 	Industrial factory
Damage Indicator (DI)	EDI-24: Electrical Transmission Line ChnDI: Utility Pole JDI-17: RC Utility Poles	EDI-18: Reinforced Concrete Structure ChnDI: Framed Residential Buildings	EDI-27: Hardwood ChnDI: Broadleaf Trees JDI-25: Broadleaf Tree	EDI-21: Steel Structure Building ChnDI: Metal-framed Industrial Buildings JDI-6: Steel Structure Factory	EDI-21: Steel Structure Building ChnDI: Metal-framed Industrial Buildings JDI-6: Steel Structure Factory
Degree of Damage (DoD)	EDI-24-DoD-5: Broken or bent steel or concrete poles ChnDoD: Non-wooden pole deflection JDI-17-DoD-1: cracking at base part	EDI-18-DoD-7: Broken window frames and interior building damage ChnDoD: Severely damaged exterior walls	EDI-27-DoD-4: Tree trunk breakage ChnDoD: Tree trunk breakage JDI-25-DoD-3: Tree trunk breakage	EDI-21-DoD-8: Total damage ChnDoD: Rigid structure collapse JDI-6-DoD-5: Complete failure of main structural frame	EDI-21-DoD-3: Metal roof or wall panels pulled from the building ChnDoD: Roof panel distortion JDI-6-DoD-3: Loss (removal, detachment)/ distortion of roofing materials
3-s Gust Speed (m/s)	EF 51-67 Chn EF 51-67 JEF 40-65	EF 49-67 Chn EF 55-75	EF 42-60 Chn EF 42-60 JEF 40-90	EF 59-80 ChnEF 54-75 JEF 80-110	EF 35-54 ChnEF 35-54 JEF 45-60
Estimated Intensity	EF3 ChnEF3 JEF2	EF2 ChnEF3	EF2 ChnEF2 JEF2	EF3 ChnEF3 JEF3	EF1 ChnEF1 JEF2

* Note: EDI – the Damage Indicators of Enhanced Fujita Scale (Texas Tech University Wind Science and Engineering Center, 2006); ChnDI – the Damage Indicators of Chinese Enhanced Fujita Scale (Tornado intensity scale: GB/T 40243-2021, 2021; Technical specifications for tornado damage, 2017); JDI – the Damage Indicators of Japanese Enhanced Fujita Scale (Japan Meteorological Agency, 2015).

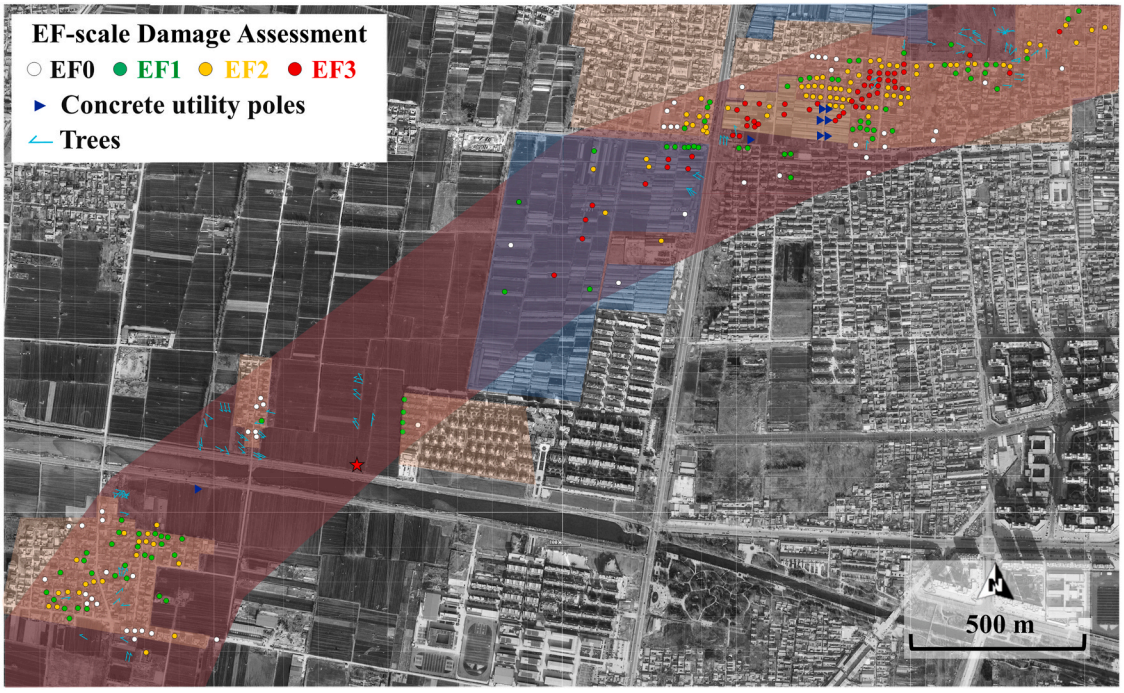

(a) Damage map in Region I (Imagery © 2025 Airbus, CNES/Airbus, Maxar Technologies, Map data © 2025)

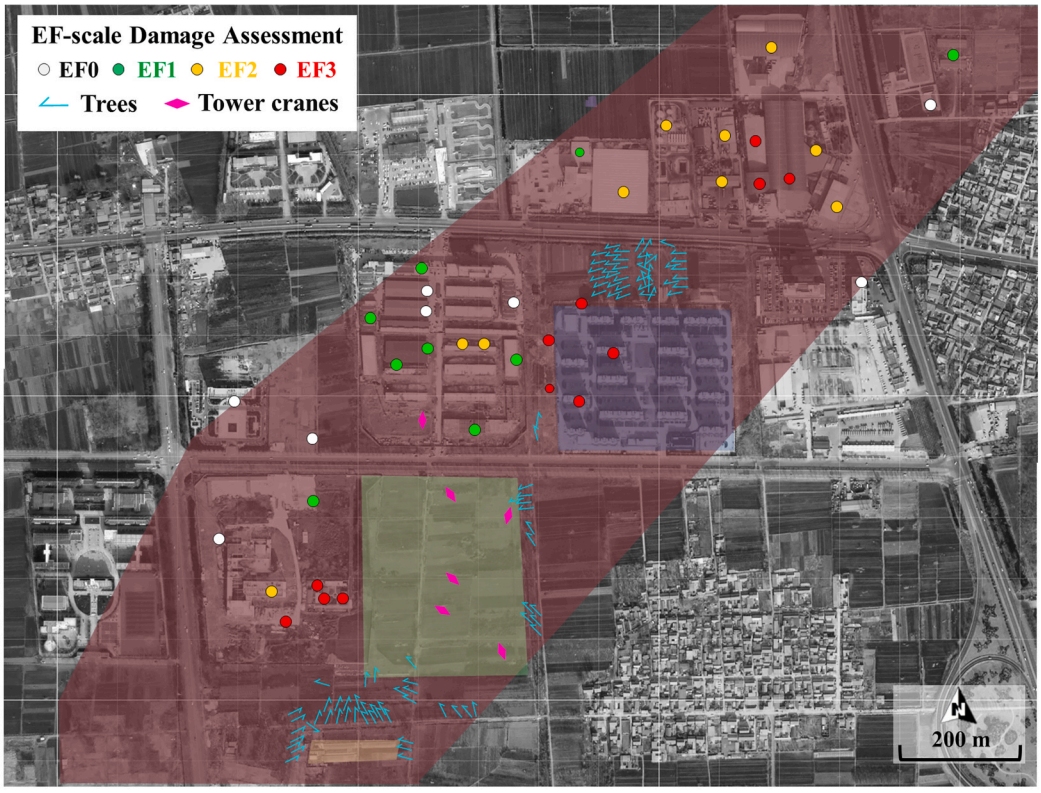

(b) Damage map in Region II (Imagery © 2025 Airbus, CNES/Airbus, Maxar Technologies, Map data © 2025)

Fig. 3. Damage locations and tornado path in Regions I and II.

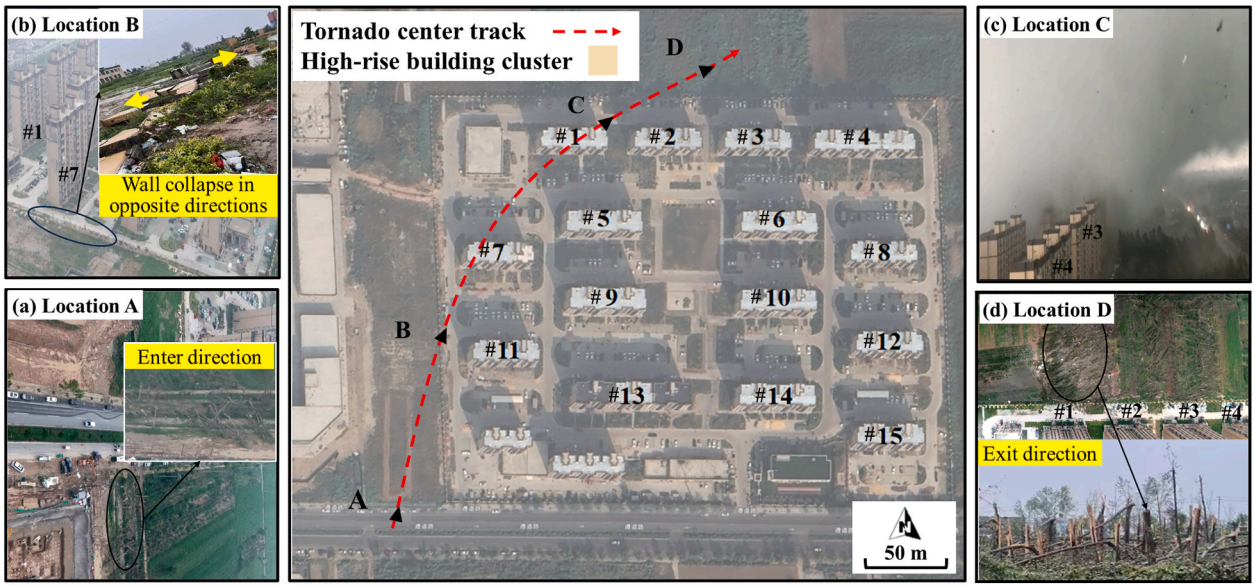

Fig. 4. Tornado center track passed over high-rise building cluster in Area ⑧.

occurred prior to failure of the frame. All damage observed on the TIL was attributed to WBD impact, which will be discussed in detail in Section 5.2. In addition to the cladding system, facade-mounted service equipment was also severely damaged, for instance, nearly all balcony-mounted solar panels and about 10% of outdoor air-conditioning units on Building #5 displaced from their original locations. These failures were evidently caused by excessive wind loading, since the anchorage systems of these objects are typically not required to sustain tornado-level winds. Once detached, these displaced objects started to act as WBD and might have caused secondary damage to the downstream buildings.

Another observation of interest from the high-rise building cluster is that the intensity of facade damage is highly correlated with the facade orientation. As shown in Fig. 5(b), in contrast to the severe damage on the south facade of Building #5 as introduced above, the north facade of the same building exhibited considerably more moderate damage. This difference is consistent with the directional characteristics of the tornado wind field. As the tornado passed over the building cluster along the track illustrated in Fig. 4, Building #5, along with the other buildings in the cluster, was primarily subjected to southeasterly winds flowing toward the tornado center. In this case, the south facades of these buildings can be generally regarded as windward, directly exposed to excessive positive wind pressure and WBD impact, whereas the north facades, as leeward, experienced relatively lower suction forces and a reduced likelihood of direct debris impact due to shielding by the building mass.

Utilizing the glass damage as an indicator to represent the damage to building facades, Fig. 6(a) presents the percentage of damaged glass area on the windward (south) facade of each building in the cluster. A clear spatial pattern is readily observed from the figure that, except for Building #1 which will be discussed later, buildings located closer to the tornado track experienced more severe damage. The four most severely damaged buildings (Buildings #5, #2, #11, and #7), each exhibiting more than 60% glass damage, are located approximately 60 m from the tornado track, whilst Building #15 at the furthest location from the track only suffered less than 10% of glass damage. According to the widely accepted analytical models for tornado-like vortices (e.g., the Rankine model (Rankine, 1882), the Burgers–Rott model (Burgers, 1948; Rott, 1958), and the Baker model (Baker and Sterling, 2017)), the tangential wind speed increases rapidly with radial distance from the vortex center, reaches its maximum at a distance known as the radius of maximum wind (RMW), and gradually decays outward. Since the damage severity is strongly correlated with wind speed, as demonstrated by numerous damage surveys and meteorological observations (Hou et al., 2025; Diao et al., 2025) and as embedded in the fundamental assumptions of the Fujita Scale (Fujita, 1981) and its enhanced versions, the RMW of the investigated tornado when it passed over the building cluster can be inferred from the observed damage distribution shown in Fig. 6(a). As discussed above, the four buildings experiencing the most severe glass damage are concentrated around a radial distance of about 60 m from the tornado track, it is reasonable to estimate that the RMW of this tornado was on the order of 60 m. It is noted that the estimated RMW involves uncertainty due to interference effect in the building clusters. This inference is generally in consistence with the findings by Brooks (2004), whose analysis of more than 4000 tornado cases indicates an RMW range of 45 to 225 m for EF3 tornadoes.

For a more detailed analysis of the damage distribution on the windward facades, each facade is divided into four equal-area segments, referred to as Segments I to IV as shown in Fig. 5(a). According to the statistics of glass damage illustrated in Fig. 6(b), a clear spatial pattern is identified that the damage in Segment IV on the eastern side is generally higher than that in the three other segments. This pattern is particularly pronounced for buildings in downstream positions (i.e., Buildings #9, #10, #5, #3, #2 and #7) compared with those in upstream positions (i.e., Buildings #13, #14, #12 and #15) under the southeasterly winds during the tornado passage. A reasonable inference is that a substantial portion of the damage in Segment IV was caused by WBD. As the winds primarily approached from the southeast during the tornado passage, buildings in downstream locations, especially in Segment IV that is near the leading edge, were more prone to WBD impact, because the upstream buildings that had already sustained severe cladding and equipment damage acted as WBD sources. This observation highlights the crucial role of building cluster layout on WBD-induced damage during extreme wind events such as tornadoes.

To investigate why the windward facade of Building #1 experienced notably less damage than those of the four other buildings located within the estimated RMW, Fig. 7 presents the field photo of the damage observed from this building. The damage observed on Building #5, as shown in Fig. 5(a), is selected for direct comparison because the two buildings have identical exterior geometry, facade configuration, and orientation, with their relative positions within the tornado wind field being the primary distinguishing factor. The survey indicates that Building #1 exhibited 7 cases of window-frame detachment failures, whereas 28 such cases were documented for Building #5. Furthermore,

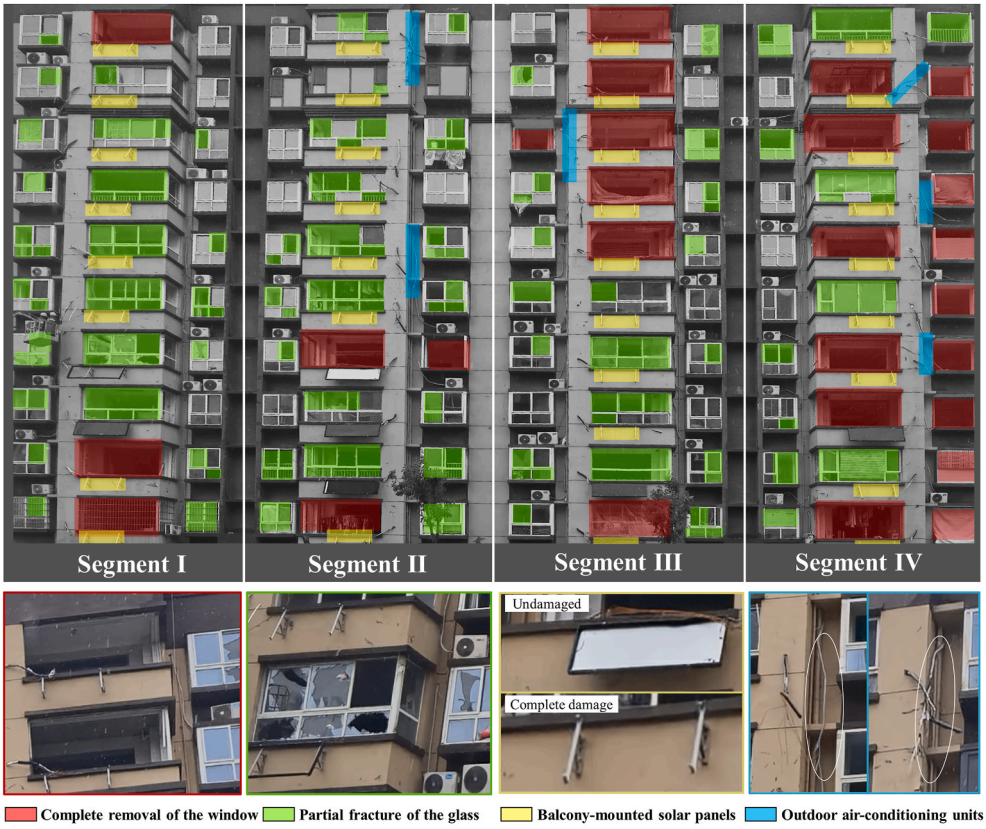

(a) Damage on south facade of Building #5



(b) Damage on north facade of Building #5

Fig. 5. Damage on facades of Building #5.

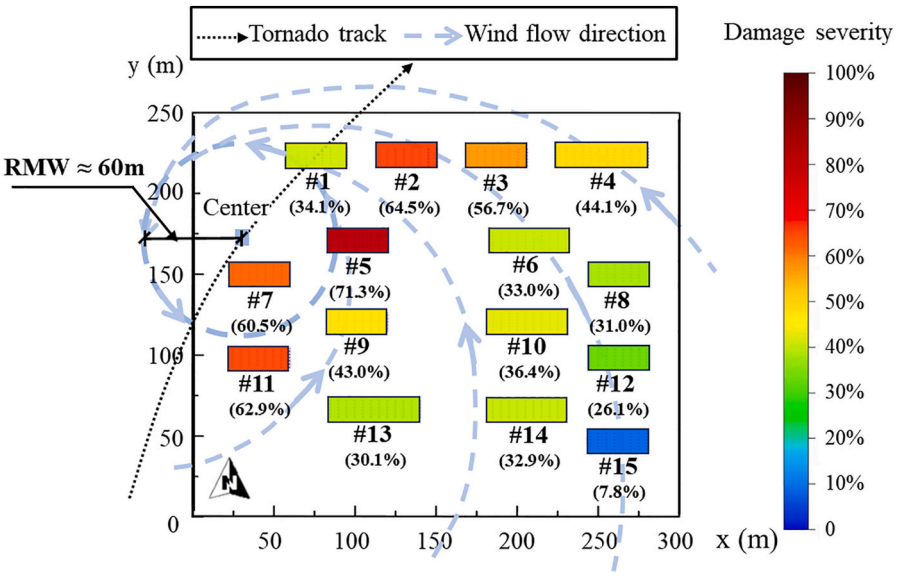

(a) Severity of damaged glass area on south facades

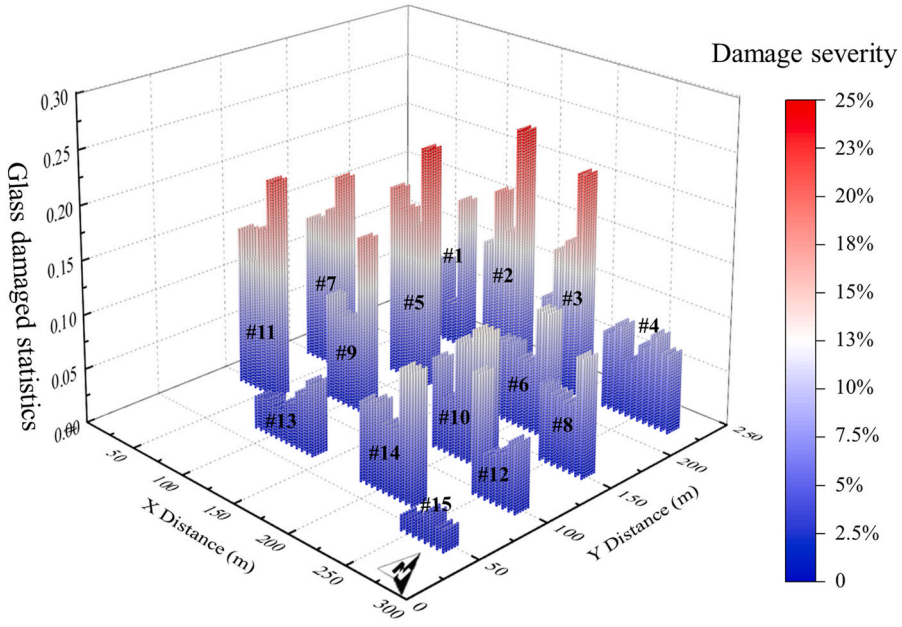

(b) Distribution of glass damage severity on south facades by regions

Fig. 6. Severity of damaged glass area on south facades of high-rise building cluster in Area ⑧

only 20 out of 40 balcony-mounted solar panels were detached from Building #1, which is significantly lower than the 33 detachments recorded for Building #5. Since these damage cases resulted clearly from excessive wind loading rather than WBD impact, the lower number of such cases on Building #1 indicates that the wind forces acting on it were substantially lower than those on Building #5. The most plausible explanation for this observation is the presence of a pronounced wind interference effect within the building cluster area. As discussed earlier, the building cluster was primarily subjected to the southeasterly winds during the tornado passage. Under this dominant wind direction, Building #5, located in the upstream position, provided substantial shielding effect on Building #1, attenuating the wind loading applied on its windward facade.

4.2. *Damage to brick-timber buildings*

The survey recorded extensive damage to brick-timber buildings in Areas ③ and ⑤, which are typically single- or two-story residential buildings characterized by load-bearing brick walls and lightweight timber gable roofs with slopes of approximately 30°. Such gable roofs are particularly vulnerable because the highly rotational and rapidly varying wind field in tornados induces complex shear and torsional loads effects, significantly increasing the risk of structural failure (Haan et al., 2010). It is noted that a large proportion of these damaged buildings were likely not properly engineered, as they were predominantly self-built decades ago without code-compliant structural detailing, and some had been vacant for years with little or no maintenance. As a result, these buildings are expected to exhibit lower wind

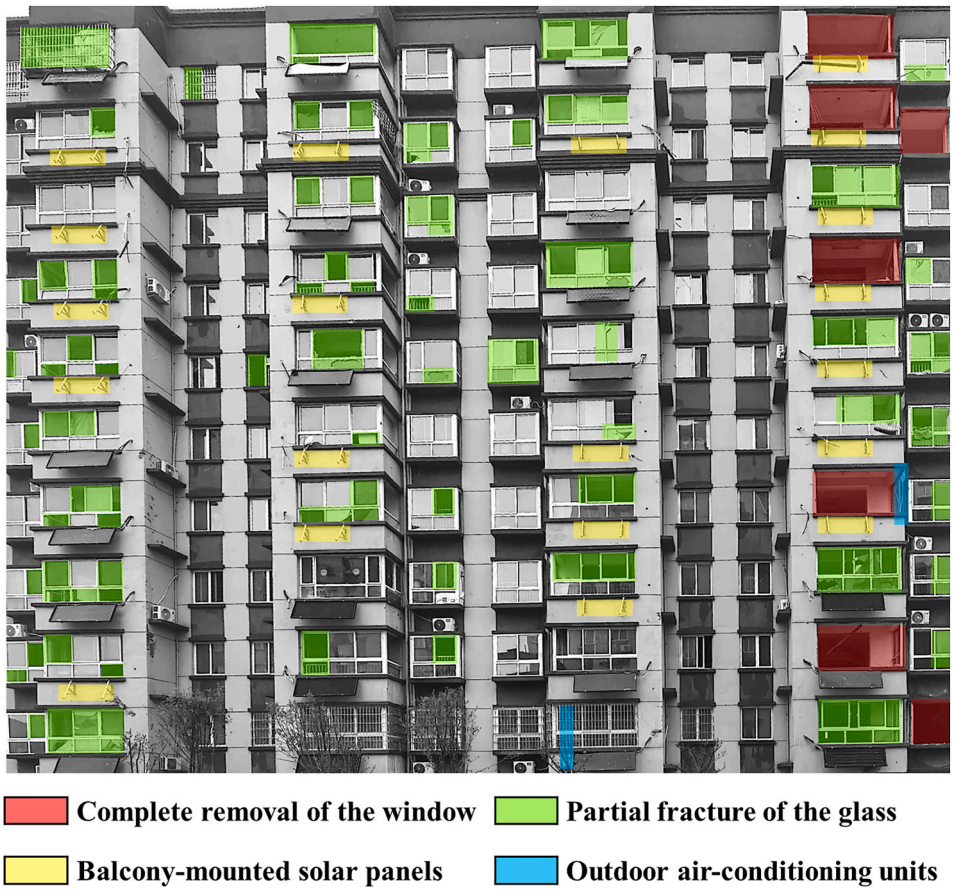

Fig. 7. Damage on south facade of Building #1.



Fig. 8. Field photos of tornado damage to brick-timber buildings.

resistance, which has been pointed out by earlier forensic studies of tornado-resistant performance in non-engineered structures (Prevatt et al., 2012; Meng et al., 2018; Yang et al., 2024). Fig. 8 presents the primary damage patterns identified from these buildings, including partial or full roof uplift as well as wall instability and collapse. Fig. 8(a) demonstrates evidence that roofing materials, clay tiles in this case, were removed by strong wind uplift pressures. Multiple roof damage cases show aerodynamic vulnerability of roofs near the eaves and corners that are subjected to strong suction due to flow separation. Meanwhile, the pressure deficit near the tornado core may further increase the uplift acting on the roof. Inadequate roof anchorage further allows the roof to be pried upward, as evident in Fig. 8(b), which is a failure mechanism commonly observed in previous tornado damage investigations (Meng et al., 2018; Yang et al., 2024; Stevenson et al., 2023). One of the most severe failure cases is shown in Fig. 8(c), where the entire roof was uplifted and part of the walls collapsed due to extreme wind forces, leading to the total failure of the building.

High wind speeds on the windward roof generate upward pulling forces, causing uplift and structural damage (see Fig. 8(a) and (b)). These aerodynamic effects were observed in the surveyed brick-timber buildings, where inadequate roof anchorage and poor roof-to-wall connections allowed the roof to be lifted and detached. As for the leeward roof, as pointed out by Haan et al. (2010), negative pressure zones are developed due to flow separation and the formation of circulation bubbles, producing strong outward suction that can lead to roof overturning. In addition to aerodynamic loading, the structural condition of the buildings also played an important role in the observed damage. Factors such as the year of construction, roof-to-wall connection details, distance from the tornado center, and WBD impacts may all have contributed to roof detachment and structural collapse (Kaushal et al., 2023).

4.3. Damage to light steel structures

Tornado damage to light steel structures, typically composed of lightweight steel frames and metal cladding, has been widely documented in literature (Meng et al., 2018; Yang et al., 2024). Unlike heavily engineered steel structures such as aircraft hangars, which often include substantial redundancy, light steel structures have limited lateral or uplift resistance, making them especially vulnerable when exposed to extreme winds that exceed their design limits.

Fig. 9 demonstrates the field photos of such damage collected in Area ⑨ corresponding to three different levels of damage, including the roof failure (Fig. 9(a)), roof and wall failure (Fig. 9(b)), and structural collapse (Fig. 9(c). As shown in Fig. 9(a), the corrugated steel roofs were torn away while the roof trusses remained generally intact, indicating that the damage was induced mainly by the excessive external pressure on the roof by flow separation. The structural failure started at the connection points between the cladding panels and the purlins, which reached their limit state under the exceeding loading during the tornado event. Previous studies also suggested a possibility that such damage may be caused by fatigue cracking around fasteners, which was observed from tropical cyclone damage cases (Tamura et al., 2022) whist this study believes that the fatigue may not be the main reason,



Fig. 9. Field photos of tornado damage to light steel structures.

given that cyclic loading during the short duration of tornado passage, typically only a few minutes, is unlikely to accumulate sufficient fatigue damage to cause connection failure. For the case in Fig. 9(b), in addition to the primary roof failure, localized wall failure was also observed as a buckling occurred on some wall girts. According to the peeling direction and deposition pattern of the roof panels, it was identified that the damaged wall girts were on the windward facade facing towards the south. The wall girts were pushed inward, suggesting that their deformation was caused by excessive positive pressure on the windward facade. This evidence indicates that the storm-relative orientation of the building significantly influences its vulnerability during a tornado event. The roof failure, in this case, is believed to be caused by the combination of external pressure which provided suction due to flow separation and the internal pressure which was boosted as the wind entered the structure through the breakage of the wall. The structure shown in Fig. 9(c) experienced major collapse with pronounced deformation of the steel frames, purlins, and cladding. A notable detail is that a part of the roof system in the middle portion remained relatively intact. This undamaged zone might be associated with local wind interference effect, related to the small-scale turbulence and building geometry, within the tornado flow field.

4.4. Damage to power distribution infrastructure systems

Tornado damage to power distribution infrastructure systems often results in substantial secondary economic loss, as industrial operations and daily activities are disrupted due to power outages. The wind damage to power grid structures mostly occur to the utility poles and transmission towers, which are slender structures sensitive to wind load.

Braik et al. (2019) found that tornado-induced unsteady flow and rapidly fluctuating pressures can excite significant dynamic responses in prestressed concrete utility poles, amplifying the requirement of structural resistance against wind load beyond those predicted by quasi-static wind analyses. In this study, multiple damage cases of utility pole were observed in Areas ③ and ⑤. These poles are hollow steel-concrete poles, with an outer diameter of 25 cm and an inner diameter of 15 cm near the bottom. The utility pole damage cases can be generally categorized by two damage patterns. The first pattern is the overturn (or leaning) as shown in Fig. 10(a), which occurs if the bearing capacity of foundations is insufficient to resist the lateral load, the overturn damage occurs. The second pattern is the break at groundline, which occurs if the ground support is adequate whilst the structural material fails to sustain the shear force. Fig. 10(b) shows a typical example of such damage, from which tension cracks near the base fracture can be clearly identified. Furthermore, other factors that reduce material capacity, such as corrosion and prestress loss, can increase the likelihood of utility pole overturning or base failure under extreme wind loads, although the forensic investigation found no evidence indicating that these factors contributed to the damage observed during the studied tornado.

Braik et al. (2019) developed a fragility models showing that the failures of prestressed concrete utility poles, which are similar to the ones observe from this field survey, initiate at wind speeds near 39 m/s (corresponding to the lower bound of wind speed range of EF1), with failure probability reaching approximately 50% at 53 m/s (EF2), and complete failure expected beyond 61 m/s (EF3 and above). This model aligns well with the observations from this survey, where utility pole damage occurred in areas exposed to estimated wind speeds of 51–67 m/s according to the EF-scale and ChnEF-scale. It is also noted that pole collapse often dragged down overhead conductors, and the weight of the collapsed or overturned (or leaning) poles will transfer to the poles next to them following the load path of the conductor lines that connect these poles, increasing the possibility of the damage of these poles next to them. It is worth noting that the WBD impact to the pole-conductor system is quite common, not only to the utility poles but also to the conductors, as shown Fig. 10(c), whilst the additional load by WBD impact is usually neglected in existing fragility models and need for further investigation.

On the other hand, transmission towers play a critical role in supporting high-voltage power lines and are engineered to withstand substantial mechanical demands, including the self-weight of conductors and continuous tensile forces during normal operation. In this survey, a transmission tower in Area ④ was found collapsed, as shown in Fig. 11. The tower legs were fractured, and pronounced bending deformation was observed, suggesting that the structure experienced severe lateral



Fig. 11. Field photo of tornado damage to a transmission tower.

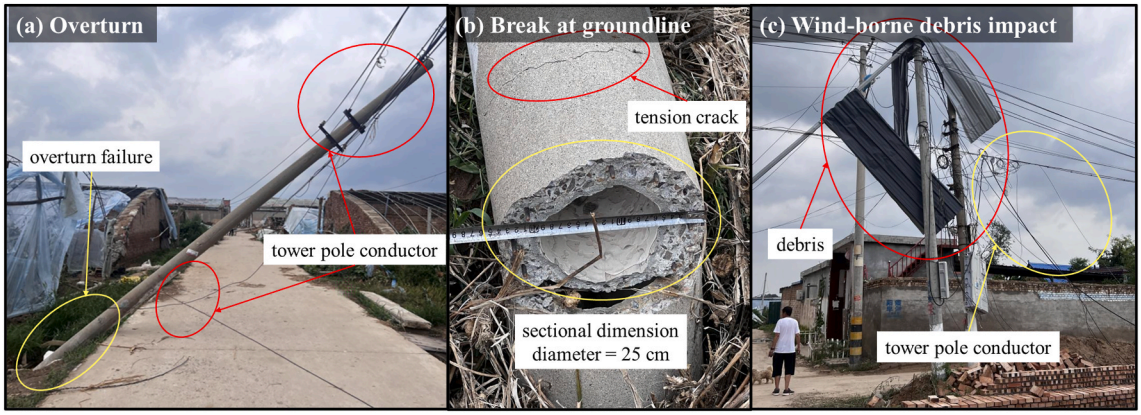

Fig. 10. Field photos of tornado damage to utility pole.

loading and associated bending and torsional demands. Under tornadic wind fields, such lateral loading can overstress slender members and connection regions, leading to buckling or fracture of critical components such as tower legs or bracing members. Failure in these primary load-carrying elements can then trigger a progressive collapse of the tower. Additionally, although no direct evidence was identified in this survey, it is recognized in prior studies that conductor motion under extreme winds can amplify dynamic forces transmitted to the tower (Hamada and El Damatty, 2016). Such effects may increase local demand at connections or bracing members and, when combined with high wind loads, could contribute to structural failure.

4.5. Damage to trees

Treefall is one of the most commonly observed forms of wind-induced damage to vegetation. In this survey, extensive treefall cases caused by the intense tornado winds were observed within the tornado path. Fig. 12 presents the treefall cases collected in Areas ⑥ and ⑧, and the estimated tornado path crossing these areas was confirmed by the video footage recorded on site as mentioned in Section 4.1.

5. Wind-borne debris motion analysis

In addition to violent winds, WBD impact is another critical reason behind the wind-related damage (Wills et al., 2002). During extreme wind events occurring in built-up areas, WBD may originate from a variety of sources, including detached roof tiles, window frames, traffic signs, tree branches, hailstones, etc. Notably, tornadoes are often accompanied by hail, and the hailstones driven by high winds may cause damage to building envelopes upon impact (Calotescu et al., 2024). However, in this study, witnesses reported no hail during the tornado event, and the survey also did not detect any hail-related damage. WBD impact essentially represents an energy-absorption problem, that is, the damage severity is governed primarily by the WBD velocity at impact, which controls the kinetic energy and momentum of the projectile. Since WBD impacts often exceed the design-level impact resistance assumed in most building codes, they constitute one of the most destructive and unpredictable mechanisms in tornado damage scenarios.

From a temporal perspective, WBD motion can be divided into three stages: lift-off, flight, and impact. In the following, Section 5.1 focuses on estimating the lift-off speed, while Section 5.2 discusses the flight and impact stages.

5.1. Estimation of lift-off speed

By estimating the lift-off speed of a given WBD, also referred to as the threshold wind speed, the lower bound of the wind intensity at the debris source location can be inferred. The lift-off speed wind speed of WBD is highly dependent on its aerodynamic properties, primarily the mass and shape, as well as on its attachment conditions to fixed objects, such as the connection between roof tiles and roof trusses. However, the mechanical performance of such connection is often highly uncertain and difficult to quantify, particularly when damage has already occurred. As a result, identifying suitable WBD cases for reliable lift-off speed estimation is challenging in post-disaster investigations. Fortunately, this survey identified a well-defined case of haybales acting as WBD in Area ②, providing a unique and suitable chance for lift-off speed analysis. Fig. 13 presents the drone-captured field photo of the site, showing the origin location of the displaced haybales, i.e., an open outdoor storage area of the farm, from which the haybales were lofted by strong winds. The haybales were uniform in cuboid geometry and mass, and they originate from the same location, which significantly reduced uncertainty in the analysis. Based on the observed information from the site, the lift-off speed of the haybales is estimated in the following.

Each haybale is categorized as a compact WBD, which is of the uniform cuboid shape measuring 60 × 40 × 30 cm (length × breadth × height) and a mass of approximately 25 kg, resulting a density of about 350 kg/m^3. Following Stevenson et al. (2023), the aerodynamic force F acting on a compact WBD is expressed by:

$$F = \frac{1}{2}\rho_a(\boldsymbol{U} - \boldsymbol{U}_m)^2 C_D A \tag{1}$$

where ρ_a denotes the air density, $\boldsymbol{U}$ denotes the wind-velocity vector, $\boldsymbol{U}_m$ denotes the WBD-velocity vector relative to the ground. It is noted that $\boldsymbol{U}$ and $\boldsymbol{U}_m$ are both vectors. A denotes the reference area of the object, and C_D denotes the drag coefficient.

For compact debris objects, assumes their rotation motion and the additional lift forces due to Magnus effect can be reasonably neglected (Baker and Sterling, 2017; Holmes, 2004). By applying Newton's Second

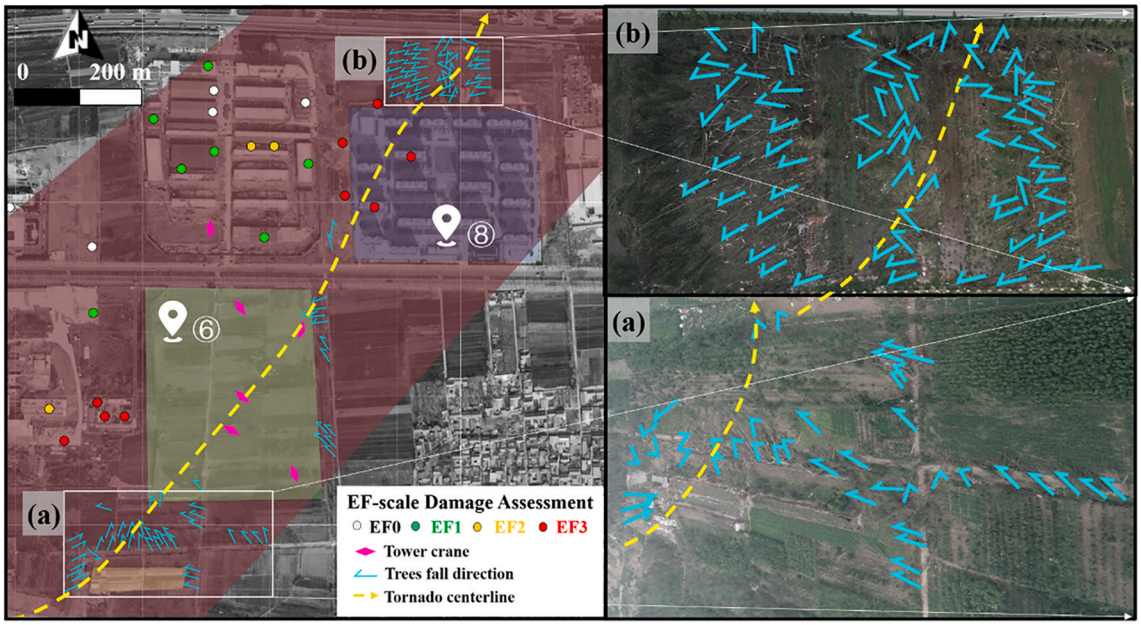

Fig. 12. Observed treefalls caused by tornado winds.

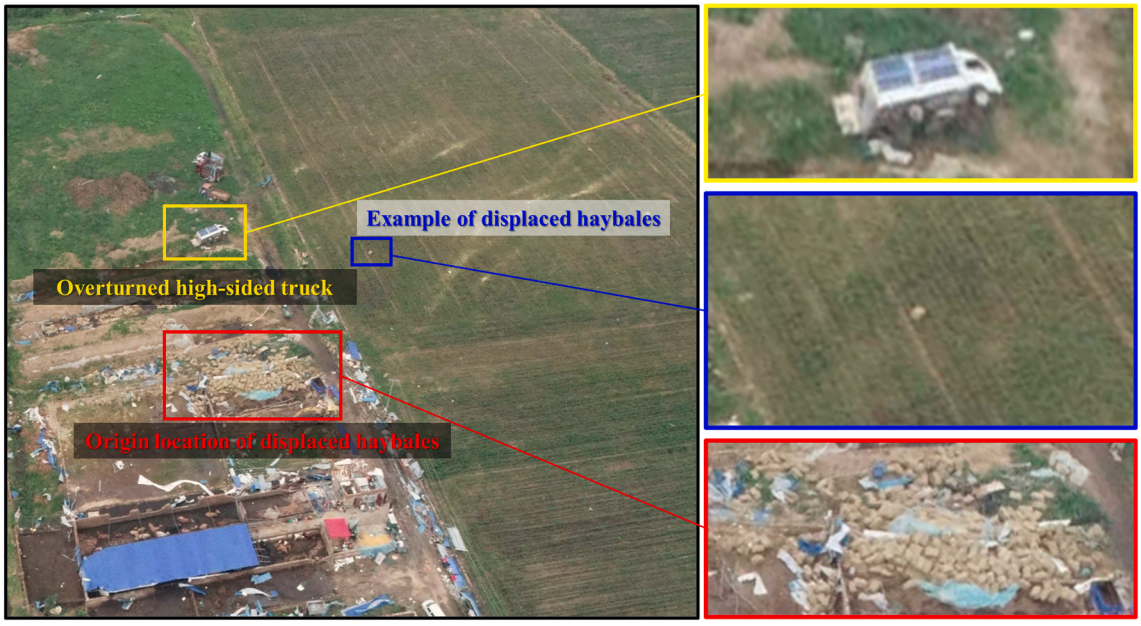

Fig. 13. Observed displaced haybales and overturned high-sided truck in Area ②

Law to the motions in both horizontal and vertical directions, the instantaneous acceleration of a compact object is given:

$$\frac{d^2x}{dt^2} = \frac{\rho_a}{2\rho_m l}(C_D \cos\alpha - C_L \sin\alpha)\left[(U_w - u_m)^2 + (V_w - v_m)^2\right] \tag{2}$$

$$\frac{d^2y}{dt^2} = \frac{\rho_a}{2\rho_m l}(C_D \sin\alpha + C_L \cos\alpha)\left[(U_w - u_m)^2 + (V_w - v_m)^2\right] - g \tag{3}$$

where $\frac{d^2x}{dt^2}$ and $\frac{d^2y}{dt^2}$ denote the horizontal and vertical acceleration of a compact object, respectively; ρ_m denotes the debris density (assumed uniform through the object); ρ_a denotes the air density; l denotes the characteristic dimension of the object, α denotes the angle between the resultant wind speed and the horizontal axis; C_L denotes the lift coefficient; U_w and V_w denotes the horizontal and vertical wind speed, respectively; u_m and v_m denotes the horizontal and vertical speeds of the object, respectively; g denotes the gravitational constant.

Assuming that the WBD does not slip before lift-off, u_m is taken as zero. At the lift-off speed, the lift force and the gravity applied to a compact object achieves equilibrium $\frac{d^2y}{dt^2} = 0$, and v_m and α are both equal to zero. Deriving from Eq. (3), the lift-off speed, $\boldsymbol{U_c}$, can be expressed by:

$$\boldsymbol{U_c} = \sqrt{{U_w}^2 + {V_w}^2} = \sqrt{\frac{2g\rho_m l}{\rho_a C_L}} \tag{4}$$

The lift and drag coefficients, C_L and C_D, conventionally determined through wind tunnel experiments, were calculated following the approach proposed by Chai et al. (2019). A shape factor parameter, S_p, is introduced to interpolate the morphology of debris objects between two prototypical geometries, namely, the ellipsoidal and cuboidal forms, expressed as follows:

$$S_p = \frac{V_{Debris} - V_{Cuboid}}{V_{Ellipsoid} - V_{Cuboid}} \tag{5}$$

where V_{Debris}, V_{Cuboid}, and $V_{Ellipsoid}$ denote the volumes of the Debris, Cuboid and Ellipsoid. Hence, S_p equals to unity and zero if the object is shaped as a perfect sphere and cube, respectively. Then, the drag and lift coefficients can be defined as follows:

$$C_{D,Debris} = (S_p)C_{D,sphere} + (1 - S_p)C_{D,cube} \tag{6}$$

$$C_{L,Debris} = (S_p)C_{L,sphere} + (1 - S_p)C_{L,cube} \tag{7}$$

Haines and Taylor (2018) and Jesson et al. (2015) suggested that, for a stationary surface-mounted cube, the ranges of C_L and C_D are 0.40 - 0.55 and 1.00 - 1.10, respectively. On the other hand, Tsutsui (2008) pointed out that for a stationary surface-mounted sphere, C_L is within the range of 0.27 - 0.35 while C_D is within 0.35 - 0.49. By substituting the above values into Eqs. (6) and (7)), C_D and C_L of the haybales were estimated to be approximately 0.99 - 1.09 and 0.40 - 0.55, respectively. Hence, following Eq. (4), it is estimated that the lift-off speed was around 55 to 65 m/s.

To validate the estimated lift-off speed, a nearby incident involving the overturning of a high-sided truck, shown in Fig. 13, was used to assess the local wind intensity. The 3-s gust speed responsible for the overturn, as estimated by the JEF, ranged from 45 to 65 m/s (Table 1), which agrees well with the lift-off speed calculated for the haybales. This close correspondence provides mutual cross-validation between the WBD-based and EF-scale-based wind speed estimates, indicating that the haybale lift-off speed was reasonably determined.

5.2. Trajectory insights from damage imprints

Due to the highly complex wind field of tornadoes, along with the aerodynamic characteristics and attachment conditions of WBD, the trajectory of an individual debris object is influenced by numerous factors and can hardly be predicted with high accuracy. Therefore, statistical analysis of WBD touchdown locations offers a more practical approach for understanding the general trajectory patterns.

In this study, the WBD impacts on a tall building in the cluster in Area ⑧, discussed in Section 4.1, were selected for further investigation. These building were clad with a TIL composed of polystyrene filler, fiberglass reinforcement mesh, and crack-resistant mortar. Owing to the deformable and energy-absorbing characteristics of the TIL system, debris impacts produced visible damage marks such as indentations across the facade surface, and in many instances, debris remained partially embedded into the TIL, offering direct evidence of debris mass, geometry, and orientation at impact, as illustrated in Fig. 14. These damage marks on the TIL provide valuable information for understanding the debris flight height and trajectory.

Fig. 15(a) illustrates the distribution of WBD damage on the east

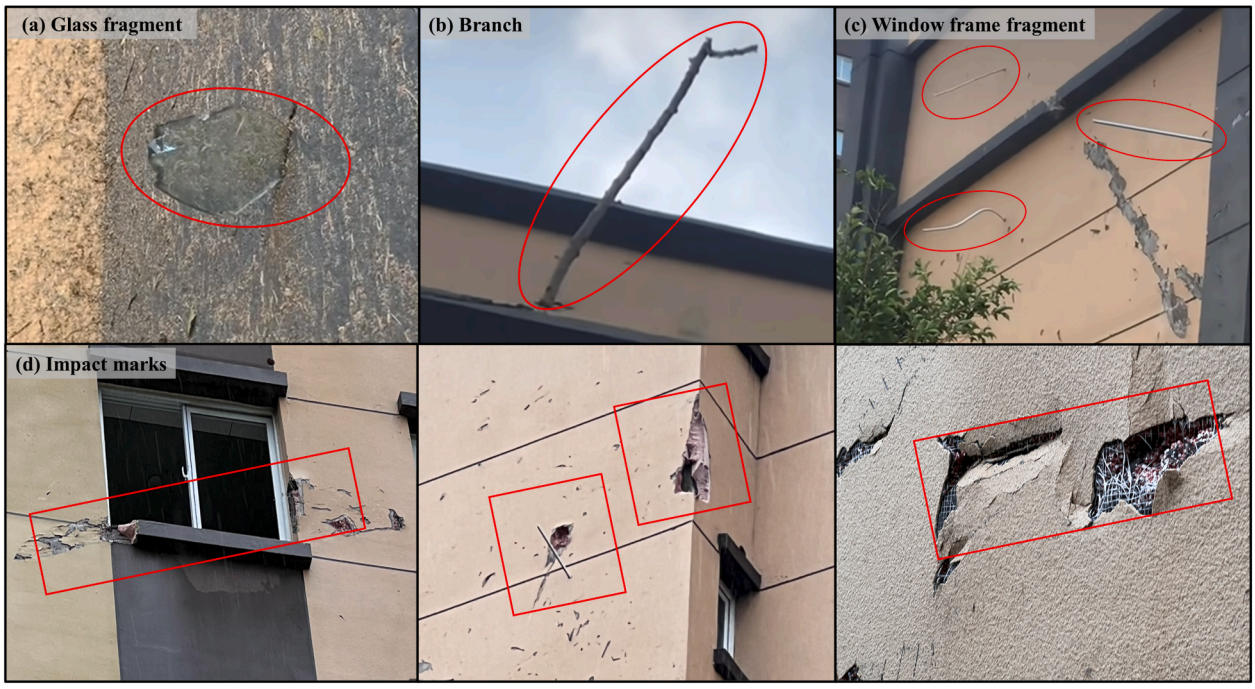

Fig. 14. WBD damage to facades of high-rise building cluster.

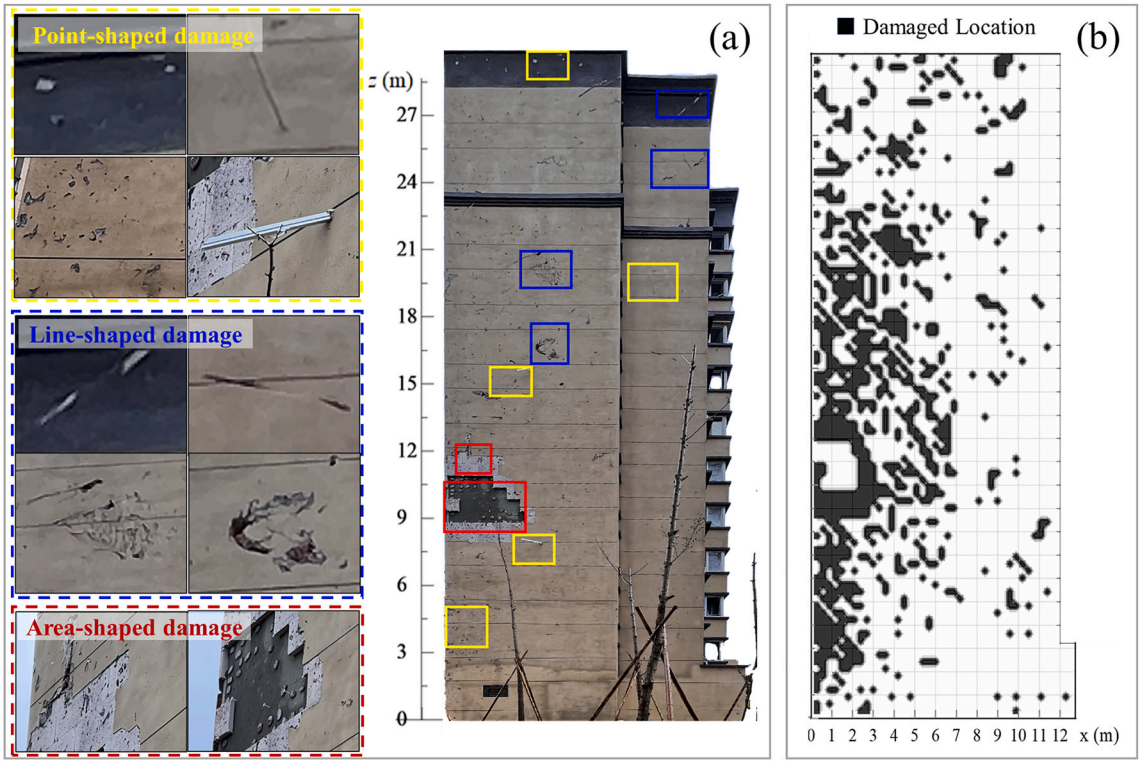

Fig. 15. Wind-borne debris damage to east facade of Building #2: (a) Damage types; (b) Spatial distribution of damage.

facade of Building #2, where three main damage imprints were documented, classified based on their geometric characteristics as point-shaped damage, line-shape damage, and area-shaped damage. Point-shaped damage refers to localized, concentrated small-size indentations, line-shaped damage corresponds to scratches or elongated grooves, and area-shaped damage indicates larger portions of the TIL material lost or detached. Field observations show that the point-shaped damage cases were caused by not only the impact of compact WBD, such as stones and bolts, but also rod-like WBD as evidences of window frame fragments embedded on the TIL were found as shown in the figure. Plate-like WBD, such as detached balcony-mounted solar panels may also cause these point-shaped damage cases, although no direct evidence was found on scene. The imprint pattern depends not only on the type of WBD, but also on its orientation and impact angle. Compact WBD

generally follows a relatively direct flight track because of its high mass-to-area ratio, while rod-like WBD may rotate or tumble during flight and produce point-shaped or line-shaped damage when its end or side strikes the facade, respectively. Plate-like WBD is more sensitive to aerodynamic forces and changes in orientation, and its fluttering or autorotational motion may produce point-shaped, line-shaped, or area-shaped damage under different impact orientations (Wills et al., 2002; Lin et al., 2007; Holmes et al., 2006). Therefore, the debris type and flight track cannot be determined solely from the geometry of an individual imprint.

Fig. 15 (b) highlights the spatial distribution of the damaged areas on the facade, showing that the majority of the damage was concentrated on the left side, namely near the southeast corner of the building. This damage pattern is consistent with the dominant southeast winds experienced by the building during the tornado event, as discussed in Section 4.1, since the WBD predominantly approached the facade from this direction. As shown in Fig. 15, the WBD-induced damage was denser and more concentrated on the left side of the facade near the southeast corner of the building. This damage pattern may be due to that Building #3, located immediately east of Building #2, partially shielded the east facade of Building #2 and from incoming WBD. Meanwhile, no clear correlation was observed between any damage imprints and the height of impact, indicating significant uncertainties associated with the WBD motion and impact behavior. This lack of a clear correlation may be attributed to the fact that the impact height is also affected by the source elevation and release condition of the WBD. Debris originating from the ground must first be lifted by the wind before reaching the upper part of the facade, whereas detached window frames, solar panels, and other facade components may begin their flight from elevated positions. In addition, the vertical wind velocity, turbulence, and flow interference among the buildings may further alter their flight tracks (Bourriez et al., 2020; Moghim et al., 2015).

6. Conclusion

This study presents a comprehensive forensic investigation of the tornado occurred in Dongming, China, on July 5th 2024, based on an extensive post-disaster field survey. The meteorological background was examined to confirm the tornadic nature of the extreme wind event, the tornado intensity was estimated using the EF scale and its adapted versions based on observed DIs and DoDs, damage to different types of structures and trees was systematically documented and the underlying damage mechanisms were analyzed, and the lift-off speed and trajectories of WBD were investigated in detail. The main findings of this paper is summarized as follows:

(1) According to the EF-scale and its Chinese and Japanese adaptations, the highest tornado intensity was assessed as EF3 based on observed damage cases across the city, which is consistent with the official report issued by the local meteorological bureau. The tornado path extended approximately 12 km, with a maximum width of roughly 690 m. Based on the spatial distribution of facade damage within the high-rise building cluster, the RMW was estimated to be approximately 60 m.
(2) Observations from a cluster of 15 high-rise buildings indicated that the damage to building facades was strongly governed by building orientation and aerodynamic interference effects. Buildings directly exposed to higher winds, due to their relative orientation to the tornado wind field, sustained more severe facade damage. In contrast, downstream buildings benefited from the shielding effect provided by upstream structures, which attenuated both wind loading and debris impact intensity. These observations underscore the critical role of building layout and inter-building aerodynamic interaction in controlling tornado-induced damage at the cluster scale.
(3) In the surveyed tornado, brick-timber building and light steel structures suffered severe damage, including major roof uplift and, in some cases, complete structural collapse. These failures were primarily caused by strong suction forces induced by flow separation, with additional contributions from factors such as inadequate connections between roofs and lower structures, limited redundancy in lateral and uplift resistance, as well as poor maintenance condition. In contrast, high-rise buildings were only affected in their facades, exhibiting substantial cladding failures, while their primary structural elements remained intact.
(4) The analysis of the haybale WBD case demonstrates the feasibility of estimating near-ground wind speeds from debris lift-off velocities, with reconstructed values of 56–66 m/s closely matching JEF-scale-based estimates of 50–61 m/s. This result highlights that, even in the absence of direct wind measurements or observable DIs for EF-scales, systematic observation of debris behavior offers a practical and reliable means to infer the intensity of extreme wind events.
(5) The observed debris imprints on the TIL-clad facades of high-rise buildings, classified as point-shaped, line-shaped, and area-shaped, provide valuable insight into WBD trajectories. The spatial distribution of WBD damage is strongly influenced by facade orientation, with areas directly exposed to the approaching winds sustaining the most severe impacts. No clear correlation was observed between any damage imprint and height, indicating the substantial uncertainties associated with WBD motion.

CRediT authorship contribution statement

Yang Lei: Writing – original draft, Software, Methodology, Investigation, Formal analysis. **Xiao Li:** Writing – review & editing, Supervision, Resources, Project administration, Methodology, Funding acquisition, Formal analysis, Conceptualization. **Guanzhong Wang:** Investigation, Data curation. **Bowen Yan:** Supervision, Conceptualization. **Xu Zhou:** Methodology, Investigation. **Qingshan Yang:** Supervision, Conceptualization. **Shenming Fu:** Methodology, Conceptualization. **Noram Irwan Ramli:** Methodology, Conceptualization. **Yingzhu Meng:** Investigation, Data curation. **Haile Li:** Investigation, Data curation.

Declaration of competing interests

The authors declare the following financial interests/personal relationships which may be considered as potential competing interests: Xiao Li reports financial support was provided by National Natural Science Foundation of China. Xiao Li reports financial support was provided by National Key Research and Development Program of China. If there are other authors, they declare that they have no known competing financial interests or personal relationships that could have appeared to influence the work reported in this paper.

Acknowledgments

The research described in this paper was financially supported by the National Natural Science Foundation of China (Grant No. 52408507) and the National Key Research and Development Program (No. 2024YFC3014101). The authors gratefully acknowledge Prof. Yukio Tamura of Chongqing University for his guidance and support in conducting the wind-related disaster field surveys.

Data availability

The data that has been used is confidential.

References

Ai, X.Q., Lyu, M.Z., Chen, J.B., 2023. Three-dimensional flight trajectories and impact damage prediction model for wind-borne debris. Nat. Hazards Rev. 24 (2), 04023005. https://doi.org/10.1061/NHREFO.NHENG-1692.

Baker, C.J., Sterling, M., 2017. Modelling wind fields and debris flight in tornadoes. J. Wind Eng. Ind. Aerod. 168, 312–321. https://doi.org/10.1016/j.jweia.2017.06.017.

Baker, C.J., Sterling, M., 2018. A conceptual model for wind and debris impact loading of structures due to tornadoes. J. Wind Eng. Ind. Aerod. 175, 283–291. https://doi.org/10.1016/j.jweia.2017.11.029.

Bourriez, F., Sterling, M., Baker, C., 2020. Windborne debris trajectories in tornado-like flow field initiated from a low-rise building. J. Wind Eng. Ind. Aerod. 206, 104358. https://doi.org/10.1016/j.jweia.2020.104358.

Braik, A.M., Koliou, M., 2025. Post-tornado automated building damage evaluation and recovery prediction by integrating remote sensing, deep learning, and restoration models. Sustain. Cities Soc. 123, 106286. https://doi.org/10.1016/j.jweia.2023.105634.

Braik, A.M., Salman, A.M., Li, Y., 2019. Risk-based reliability and cost analysis of utility poles subjected to tornado hazard. J. Aero. Eng. 32 (4), 04019040. https://doi.org/10.1061/(ASCE)AS.1943-5525.0001029.

Brooks, H.E., 2004. On the relationship of tornado path length and width to intensity. Weather Forecast. 19 (2), 310–319. https://doi.org/10.1175/1520-0434(2004)019%3C0310:OTROTP%3E2.0.CO;2.

Burgers, J.M., 1948. A mathematical model illustrating the theory of turbulence. Adv. Appl. Mech. 1, 171–199. https://doi.org/10.1016/S0065-2156(08)70100-5.

Calotescu, I., Li, X., Mengistu, M.T., Repetto, M.P., 2024. Thunderstorm impact on the built environment: a full-scale measurement and post-event damage survey case study. J. Wind Eng. Ind. Aerod. 245, 105634. https://doi.org/10.1016/j.jweia.2023.105634.

Chai, V., Parkhi, D., Boopathy, S., Xiang, J., Schlüter, J., 2019. A model for the aerodynamic coefficients of rock-like debris. C. R. Mec. 347 (1), 19–32. https://doi.org/10.1016/j.crme.2018.10.001.

Chmielewski, T., Nowak, H., Walkowiak, K., 2013. Tornado in Poland of August 15, 2008: results of post-disaster investigation. J. Wind Eng. Ind. Aerod. 118, 54–60. https://doi.org/10.1016/j.jweia.2013.04.007.

Diao, X.G., Meng, X.G., Zhu, X.Q., Han, Y.Q., 2025. Radar observation characteristics of tornado outbreak events in Shandong on 5 July 2024. J.Marine Meteorol. 45 (2), 14–27. https://doi.org/10.19513/j.cnki.hyqxxb.20241031001, 2025.

Doswell, I.I.I.C.A., Carbin, G.W., Brooks, H.E., 2012. The tornadoes of spring 2011 in the USA: an historical perspective. Weather 67 (4), 88–94. https://doi.org/10.1002/wea.1902.

EMDAT, 2023. Center for research on the epidemiology of disasters. https://public.emdat.be/data. (Accessed 31 May 2025).

Esri, 2023. Matador, Texas tornado. ArcGIS StoryMaps. https://storymaps.arcgis.com/stories/8df884dbd4e849c89d4b1128fa5dc1d6. (Accessed 31 May 2025).

Fujita, T.T., 1981. Tornadoes and downbursts in the context of generalized planetary scales. J. Atmos. Sci. 38 (8), 1511–1534. https://doi.org/10.1175/1520-0469(1981)038%3C1511:TADITC%3E2.0.CO;2.

Godfrey, C.M., Peterson, C.J., 2017. Estimating enhanced Fujita scale levels based on forest damage severity. Weather Forecast. 32 (1), 243–252. https://doi.org/10.1175/WAF-D-16-0104.1.

Grieser, J., Haines, P., 2020. Tornado risk climatology in Europe. Atmosphere 11 (7), 768. https://doi.org/10.3390/atmos11070768.

Haan Jr., F.L., Balaramudu, V.K., Sarkar, P.P., 2010. Tornado-induced wind loads on a low-rise building. J. Struct. Eng. 136 (1), 106–116. https://doi.org/10.1061/(ASCE)ST.1943-541X.0000093.

Haan Jr., F.L., Sarkar, P.P., Kopp, G.A., Stedman, D.A., 2017. Critical wind speeds for tornado-induced vehicle movements. J. Wind Eng. Ind. Aerod. 168, 1–8. https://doi.org/10.1016/j.jweia.2017.04.014.

Haines, M., Taylor, I., 2018. Numerical investigation of the flow field around low rise buildings due to a downburst event using large eddy simulation. J. Wind Eng. Ind. Aerod. 172, 12–30.

Hamada, A., El Damatty, A.A., 2016. Behaviour of transmission line conductors under tornado wind. Wind Struct.Int. J. 22 (3), 369–391. https://doi.org/10.12989/was.2016.22.3.369.

Holmes, J.D., 2004. Trajectories of spheres in strong winds with application to wind-borne debris. J. Wind Eng. Ind. Aerod. 92 (1), 9–22. https://doi.org/10.1016/j.jweia.2003.09.031.

Holmes, J.D., Letchford, C.W., Lin, N., 2006. Investigations of plate-type windborne debris—Part II: computed trajectories. J. Wind Eng. Ind. Aerod. 94 (1), 21–39. https://doi.org/10.1016/j.jweia.2005.10.002.

Hou, S.M., Meng, X.G., Guo, Z.Y., Li, Y.W., Zhu, X.Q., Xin, Y., 2025. Small- and meso-scale characteristics of "24·7" clustered tornado process in Shandong. J.Marine Meteorol. 45 (2), 28–40. https://doi.org/10.19513/j.cnki.hyqxxb.20241025001, 2025.

Jain, A., Bhusar, A.A., Roueche, D.B., Prevatt, D.O., 2020. Engineering-based tornado damage assessment: numerical tool for assessing tornado vulnerability of residential structures. In: Frontiers in Built Environment, 6, p. 89. https://doi.org/10.3389/fbuil.2020.00089.

Japan Meteorological Agency, 2015. Guidelines for the Japanese enhanced Fujita Scale. http://www.data.jma.go.jp/obd/stats/data/bosai/tornado/kentoukai/kaigi/2015/1221_kentoukai/guideline.pdf.

Jesson, M., Sterling, M., Letchford, C., Haines, M., 2015. Aerodynamic forces on generic buildings subject to transient, downburst-type winds. J. Wind Eng. Ind. Aerod. 137, 58–68.

Karstens, C.D., Gallus Jr, W.A., Lee, B.D., Finley, C.A., 2013. Analysis of tornado-induced tree fall using aerial photography from the Joplin, Missouri, and Tuscaloosa–Birmingham, Alabama, tornadoes of 2011. J. Appl. Meteorol. Climatol. 52 (5), 1049–1068. https://doi.org/10.1175/JAMC-D-12-0206.1.

Kaushal, S.S., Soto, M.G., Napolitano, R., 2023. Understanding the performance of historic masonry structures in Mayfield, KY after the 2021 tornadoes. J. Cult. Herit. 63, 120–134. https://doi.org/10.1016/j.culher.2023.07.002.

Li, X., Yu, X., Li, Q.S., Allsop, A., 2021. Field measurement and validation of structural dynamic parameters of skyscrapers under super typhoon excitation. J. Civil Struct. Health Monitor. 11 (3), 609–627. https://doi.org/10.1007/s13349-021-00470-3.

Lin, N., Holmes, J.D., Letchford, C.W., 2007. Trajectories of wind-borne debris in horizontal winds and applications to impact testing. J. Struct. Eng. 133 (2), 274–282. https://doi.org/10.1061/(ASCE)0733-9445(2007)133:2(274.

Lombardo, F.T., Roueche, D.B., Prevatt, D.O., 2015. Comparison of two methods of near-surface wind speed estimation in the 22 May, 2011 Joplin, Missouri Tornado. J. Wind Eng. Ind. Aerod. 138, 87–97. https://doi.org/10.1016/j.jweia.2014.12.007.

Meng, Z., Bai, L., Zhang, M., Wu, Z., Li, Z., Pu, M., Li, L., 2018. The deadliest tornado (EF4) in the past 40 years in China. Weather Forecast. 33 (3), 693–713. https://doi.org/10.1175/WAF-D-17-0085.1.

Miller, C.S., Kopp, G.A., Sills, D.M., Butt, D.G., 2024. Estimating wind speeds in tornadoes using debris trajectories of large compact objects. Mon. Weather Rev. 152 (8), 1859–1881. https://doi.org/10.1175/MWR-D-23-0251.1.

Moghim, F., Xia, F.T., Caracoglia, L., 2015. Experimental analysis of a stochastic model for estimating wind-borne compact debris trajectory in turbulent winds. J. Fluid Struct. 54, 900–924. https://doi.org/10.1016/j.jfluidstructs.2015.02.007.

National Weather Service (NWS), 2023. Natural hazard statistics. https://www.weather.gov/hazstat/. (Accessed 3 June 2025).

NOAA, 2023. U.S. Tornado Climatology. National Oceanic and Atmospheric Administration. https://www.ncei.noaa.gov/access/monitoring/tornadoes/. (Accessed 1 June 2025).

Prevatt, D.O., Coulbourne, W., Graettinger, A.J., et al., 2012. Joplin, Missouri, Tornado of May 22, 2011: Structural Damage Survey and Case for tornado-resilient Building Codes[M]. American Society of Civil Engineers (ASCE). https://doi.org/10.1061/9780784412503.

Rankine, W.J.M., 1882. A Manual of Applied Physics, Vol. 663, 10th Ed. Charles Griff and Co, London.

Rott, N., 1958. On the viscous core of a line vortex. Zeitschrift für angewandte Mathematik und Physik ZAMP 9 (5), 543–553. https://doi.org/10.1007/BF02424773.

Rotunno, R., Bluestein, H.B., 2024. Recent developments in tornado theory and observations. Rep. Prog. Phys. 87 (11), 114801. https://doi.org/10.1088/1361-6633/ad7f6a.

Sills, D.M., Kopp, G.A., Elliott, L., Jaffe, A.L., Sutherland, L., Miller, C.S., et al., 2020. The northern tornadoes project: uncovering Canada's true tornado climatology. Bull. Am. Meteorol. Soc. 101 (12), E2113–E2132. https://doi.org/10.1175/BAMS-D-20-0012.1.

Sills, D.M., McCarthy, P.J., Kopp, G.A., 2014. Implementation and application of the EF-scale in Canada. In preprints, 27th conf. on severe local storms. Madison, WI, Amer. Meteor. Soc. B 16.

Simiu, E., Potra, F.A., 2011. Technical basis for regulatory guidance on design-basis hurricane-borne missile speeds for nuclear power plants. NUREG/CR-7004 [online]. https://tsapps.nist.gov/publication/get_pdf.cfm?pub_id=907911. (Accessed 16 December 2025).

Stevenson, S.A., Miller, C.S., Sills, D.M., Kopp, G.A., Rhee, D.M., Lombardo, F.T., 2023. Assessment of wind speeds along the damage path of the Alonsa, Manitoba EF4 tornado on 3 August 2018. J. Wind Eng. Ind. Aerod. 238, 105422. https://doi.org/10.1016/j.jweia.2023.105422.

Tamura, Y., Yang, Q., Wang, Y., 2022. Design of temporary, conditional, general and highly influential buildings for tropical cyclones and severe local storms. Adv. Struct. Eng. 25 (16), 3215–3234. https://doi.org/10.1177/13694332221135905.

Technical Specifications for Tornado Damage Investigation: GB/T 34301-2017, 2017. Standards Press of China, Beijing.

Texas Tech University Wind Science and Engineering Center, 2006. A Recommendation for an Enhanced Fujita Scale (EF-scale). National Weather Service. http://www.spc.noaa.gov/faq/tornado/ef-ttu.pdf.

Tornado intensity scale: GB/T 40243-2021, 2021. National Meteorological Disaster Prevention and Mitigation Standardization Technical Committee (SAC/TC 345). Standards Press of China [in Chinese].

Tsutsui, T., 2008. Flow around a sphere in a plane turbulent boundary layer. J. Wind Eng. Ind. Aerod. 96 (6–7), 779–792.

Wills, J.A.B., Lee, B.E., Wyatt, T.A., 2002. A model of wind-borne debris damage. J. Wind Eng. Ind. Aerod. 90 (4–5), 555–565. https://doi.org/10.1016/S0167-6105(01)00197-0.

Xu, B.L., Zhao, S.H., Qiu, P.H., et al., 2024. Study on risk zoning of tornado disaster in China. Building Structure 54 (2), 110–114. https://doi.org/10.19701/j.jzjg.20210947 [in Chinese].

Yang, Q., Yin, J., Liu, M., Wang, Y., Hui, Y., Li, S., et al., 2024. Post-disaster investigations of damage feature of buildings and structures due to several local strong winds in China during 2021–2024. Adv. Wind Eng. 1 (2), 100011. https://doi.org/10.1016/j.awe.2024.100011.

Zhang, N.L., Qiu, G., Tan, X., Chen, J., Sun, R., Wu, B.J., Cheng, X.X., 2024. Structural response of a large transmission Tower to a tornado in East China. Shock Vib. 2024 (1), 9103526. https://doi.org/10.1155/2024/9103526.